ACS APPLIED MATERIALS & INTERFACES

RESEARCH ARTICLE

www.acsami.org

Low-Temperature UV Processing of Nanoporous SnO_2 Layers for Dye-Sensitized Solar Cells

Zoe Tebby,[†] Tamez Uddin,[†] Yohann Nicolas,[†] Céline Olivier,[†] Thierry Toupance,[†,*] Christine Labrugère,[‡] and Lionel Hirsch[§]

[†]University of Bordeaux 1, Institut des Sciences Moléculaires, Groupe C2M, UMR 5255 CNRS, 351 Cours de la Libération, F-33405 Talence Cedex, France

[‡]CeCaMA (Centre de Caractérisation des Matériaux Avancés), Institut de Chimie de la Matière Condensée de Bordeaux, UPR 9048 CNRS, Château Brivazac, Avenue du Docteur A. Schweitzer, F-33608 Pessac Cedex, France

[§]Laboratoire de l'Intégration du Matériau au Système, UMR 5218 CNRS, ENSCBP, 16 Avenue Pey-Berland, 33607 Pessac Cedex, France

ABSTRACT: Connection of SnO_2 particles by simple UV irradiation in air yielded cassiterite SnO_2 porous films at low temperature. XPS, FTIR, and TGA-MS data revealed that the UV treatment has actually removed most of the organics present in the precursor SnO_2 colloid and gave more hydroxylated materials than calcination at high temperature. As electrodes for dye-sensitized solar cells (DSCs), the N3-modified 1−5 μm thick SnO_2 films showed excellent photovoltaic responses with overall power conversion efficiency reaching 2.27% under AM1.5G illumination (100 mW cm^{-2}). These performances outperformed those of similar layers calcined at 450 °C mostly due to higher V_{oc} and FF. These findings were rationalized in terms of slower recombination rates for the UV-processed films on the basis of dark current analysis, photovoltage decay, and electrical impedance spectroscopy studies.

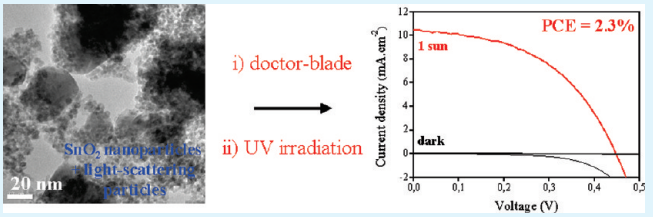

KEYWORDS: tin dioxide, low-temperature processing, UV irradiation, dye-sensitized solar cells

INTRODUCTION

Since the pioneering works of O'Regan and Grätzel,[1] dye-sensitized solar cells (DSCs) have attracted considerable worldwide attention over the past 15 years because they show many advantages such as a low-cost, easy manufacturing processing, environmental compatibility, transparency, tunable color, and rather high energy conversion efficiencies that are comparable to those of amorphous silicon cells.[2] The best system reported up to now, with overall power conversion efficiencies reaching 11.2% under AM1.5 illumination,[3] are built from nanoporous anatase titanium dioxide (TiO_2) films processed at high temperature on glass substrates, the surface of which is chemically modified with ruthenium dye complexes endowed with carboxylic acid groups, in contact with an electron donor liquid electrolyte. Furthermore, significant advances have been recently achieved in the field of DSC modules with certified efficiencies of about 8.2%.[4] On the other hand, with the fast development of modern portable electronic devices that necessitates renewable flexible power sources,[5] different low-temperature processing routes of TiO_2 layers have been investigated to process flexible DSCs.[6−18] The compression method gave the best performance described so far for small active areas (0.2 cm^2) with a conversion yield of 7.4% on ITO/plastic substrate,[16c] whereas the electrophoretic deposition (EPD) method associated with a pressure post-treatment yielded very interesting efficiencies (6.2%) for larger active areas (0.65 cm^2).[17] However, TiO_2-based systems still suffer from some limitations due to high electron recombination rates related to the low electron mobility and transport properties of TiO_2[19] and stability problems mainly under UV light.

Compared to TiO_2, tetragonal tin dioxide (SnO_2) is a promising wide band gap oxide material for such an application because of its outstanding chemical and physical properties.[20] Thus, it is a better electron acceptor because of a more positive conduction band edge that should enhance electron transfer rates from photoexcited dye molecules, if this process is a limiting factor. Moreover, SnO_2 shows much higher electronic mobility and has a lower sensitivity to UV degradation due to its larger band gap (3.7 eV) that should confer better long-term stability to the corresponding cells. However, the best efficiencies reported so far for pure SnO_2-based DSCs remain low, around 1.5% under AM1.5G illumination (100 mW cm^{-1}),[21] in spite of attempts made to improve dye-oxide linkage,[22] crystallinity,[23] morphology,[24] or porosity of the nanoparticulate-SnO_2 layers[21] or to enhance the open-circuit photovoltage of such systems by band-edge engineering.[25] Higher efficiencies were only reached with SnO_2-based electrodes, including TiO_2 coatings[26] or ZnO particles.[27] Moreover, to the best of our knowledge, no effort has been devoted to low-temperature processing nanoparticulate SnO_2-based DSCs compatible with flexible plastic substrates.

Received: January 14, 2011
Accepted: March 28, 2011
Published: March 28, 2011

Table 1. Textural Properties of the SnO_2 Powders Used in this Work

SnO_2 source	structure	crystallite size (nm)[a]	particle size (nm)[b]	S_{BET} ($m^2\ g^{-1}$)[c]
Alfa Aesar	Cassiterite	4	5	155 ± 4.5
Aldrich	Cassiterite	>100	10−300	7 ± 0.5

[a] From the XRD pattern using the Scherrer equation (±0.5 nm). [b] From TEM images (±0.5 nm). [c] From N_2 sorption measurements.

Recently, we have reported the UV processing of anatase TiO_2 nanoporous films at low temperature for plastic electrochromic devices[28] or DSCs,[29] and this method may be generalized to other semiconducting oxides. We hereafter describe the extension of this method to the preparation of cassiterite SnO_2 porous electrodes and the characterization of DSCs based on these layers. Our studies clearly showed that the UV-sintering method without any additional post-treatment provided SnO_2 photoanodes leading to higher conversion energy efficiencies than the best results reported in the literature for pure SnO_2 porous electrodes annealed at high temperature. The performances of the UV-treated electrodes stem from higher V_{oc} and FF and were rationalized in terms of slower recombination rates.

EXPERIMENTAL SECTION

Materials. Commercial SnO_2 colloid (15% SnO_2 in H_2O, pH 9.5−10.5; counterion: K^+; Alfa Aesar) and large light-scattering SnO_2 (−325 mesh, Aldrich) particles were used as supplied. Triton X-100 (Aldrich), acetone (VWR), acetic acid (Lancaster), bis(isothiocyanato) ruthenium(II)-bis-2,2′-bipyridine-4,4′-dicarboxylic acid (hereafter named N3, Dyesol), and liquid electrolyte (iolitec, IoLilyte(R)SP-382: 0.8 M 1-methyl-3-propylimidazolium iodide; 0.15 M I_2; 0.5 M N-methylbenzimidazole and 0.1 M guanidinium thiocyanate in 3-methoxyvaleronitrile)[30] were employed without any further purification. The conductive substrates, F-doped SnO_2/glass (10 Ω/square, Solems), were first cleaned by sonication in a detergent solution (Hellmanex) for 15 min followed by UV−ozone treatment for 1 h. The textural properties of the particles used in this study are reported in Table 1.

Processing of Tin Dioxide Porous Films. The colloidal suspensions were prepared as follows: 3.33 g of the Alfa Aesar colloid and 0.85 g of light scattering particles (Aldrich) were dispersed into a mixture of water (1−7 mL) and acetone (2 mL) in the presence of Triton X-100 (10 drops) and acetic acid (2 drops). The colloids were coated over the substrates with a glass rod between single strips of 3 M Magic Tape (thickness of 40 μm) placed along the substrate edges. After drying at room temperature, the layers were exposed for 3 h to UV irradiation (vapor Hg lamp (Philips HPL-N) emitting 365 and 254 nm wavelengths, 125 W), and for comparison, films were dried at 150 °C for 2 h (hereafter LT films) or annealed in air for 30 min at 450 °C (hereafter HT films).

Sample Characterization. The film thickness was determined by SEM (Hitachi Tabletop microscope TM-1000). HR-SEM images were recorded with a JEOL JSM-6700F microscope. Nitrogen sorption (BET) analyses were carried out with Micromeritics ASAP 2010, either on powder or on large quantities (≈100 mg) of films scraped off the substrate. TGA-MS were performed on a Netzsch STA409 simultaneous analyzer coupled with a Thermostar GSD 300T3 Balzers Instruments mass spectrometer. XPS spectra were recorded with a 220i-XL ESCALAB from VG equipped with a Mg Kalpha (1253.6 eV) X-ray source. The spectra were calibrated in relation to the $Sn(3d_{5/2})$ binding energy (486.7 ± 0.1 eV), which was applied as an internal standard. Fittings of the high resolution spectra were provided through the AVANTAGE software from ThermoFischer Scientific. FTIR measurements were carried out with a Perkin-Elmer spectrum 100 FT-IR spectrophotometer using a MIRacle ATR platform from PIKE Technonolgies.

Cell Fabrication and Photovoltaic Measurements. Immersion of the electrodes in a 0.5 mM solution of the N3 dye in a mixture of acetonitrile and tert-butyl alcohol (v:v = 1:1) at RT for 48 h provided N3-sensitized photoanodes. A 40 μm spacer with a hole in the middle was stuck onto a Pt-sputtered FTO/glass counter-electrode. The liquid electrolyte was deposited on the bare part, the dye-sensitized electrode was placed on top, and then the system was sealed. The active area (0.2 cm^2) was delimited by an aluminum device with screws enabling to hold the two components of the cell together. The cell was illuminated by a AM1.5G solar simulator calibrated with a radiometer (IL 1400BL), and the I−V responses were measured with a Keithley 4200 semiconductor analyzer. The incident photon to charge carrier efficiency (IPCE) data were collected each nanometer from 300 to 1000 nm using an Xe lamp associated with a monochromator (Triax 180, Jobin Yvon). No bias light was employed to illuminate the cell. The current produced was measured by steps of 1 nm after 200 ms of radiation exposure with a Keithley 6487 picoammeter in order to be in steady state conditions. The incident photon flux was measured with a 6 in. diameter calibrated integrated sphere (Labsphere) and a silicon detector. Electrical impedance spectra were recorded with an Autolab PGSTAT100 potensiostat galvanostat (Methrom) under 100 mW cm^{-2} illumination. Impedance data were measured at open-circuit voltage of the devices, the frequency varying from 10^5 to 10^{-2} Hz, and the voltage amplitude was 20 mV. Photovoltage rise and decay measurements were carried out by illuminating the DSCs with a green diode (emission: 550 nm) monitored with a tension generator (Centrad, GF266). The resulting signals were recorded with an oscilloscope (Tetronilx, TDS2014).

RESULTS AND DISCUSSION

Thin Film Preparation and Characterization. Porous nanocrystalline oxide photoelectrodes are traditionally prepared at high temperature from colloids containing metal oxide nanoparticles and organic binders or additives. The latter are generally considered as crucial to control the agglomeration of the nanoparticles, to reduce the stress, and to create voids during the thermal post-treatments in order to obtain crack-free layers with an optimal meso- and macroporous structure. However, low-temperature processing routes preclude the use of high molecular organic binders that cannot be completely eliminated from the photoanodes. Preliminary studies revealed that well-adherent films thicker than 1 μm could not be processed from the Alfa Aesar SnO_2 colloids by the "doctor-blading" technique combined with a UV post-treatment. As a result, the addition of light-scattering SnO_2 particles was required to get suitable photoanodes for DSCs. Thus, crack-free and homogeneous films were obtained after coating by the "doctor-blade" technique followed by UV irradiation. By tuning the concentration of the SnO_2 particles in the colloid, the film thickness could be varied in the range 1−5 μm. SEM images of the layers prepared indicate the formation after UV treatment of porous films made of aggregated particles as depicted in panels (A) and (B) of Figure 1. By contrast, sintering at 450 °C led to less porous films with some cracks (Figure 1C,D). Furthermore, N_2 sorption measurements carried out on films scraped off confirmed that the most porous layers were obtained after UV treatment (Table 2). Indeed, the BET surface area and total pore volume of about 61 $m^2\ g^{-1}$ and 0.13 $cm^3\ g^{-1}$, respectively, were measured for UV-processed films. As a result, the BET specific surface area matched very well with that expected from a mixture of Alfa Aesar SnO_2 particles and light scattering particles that reveals that no sintering effect

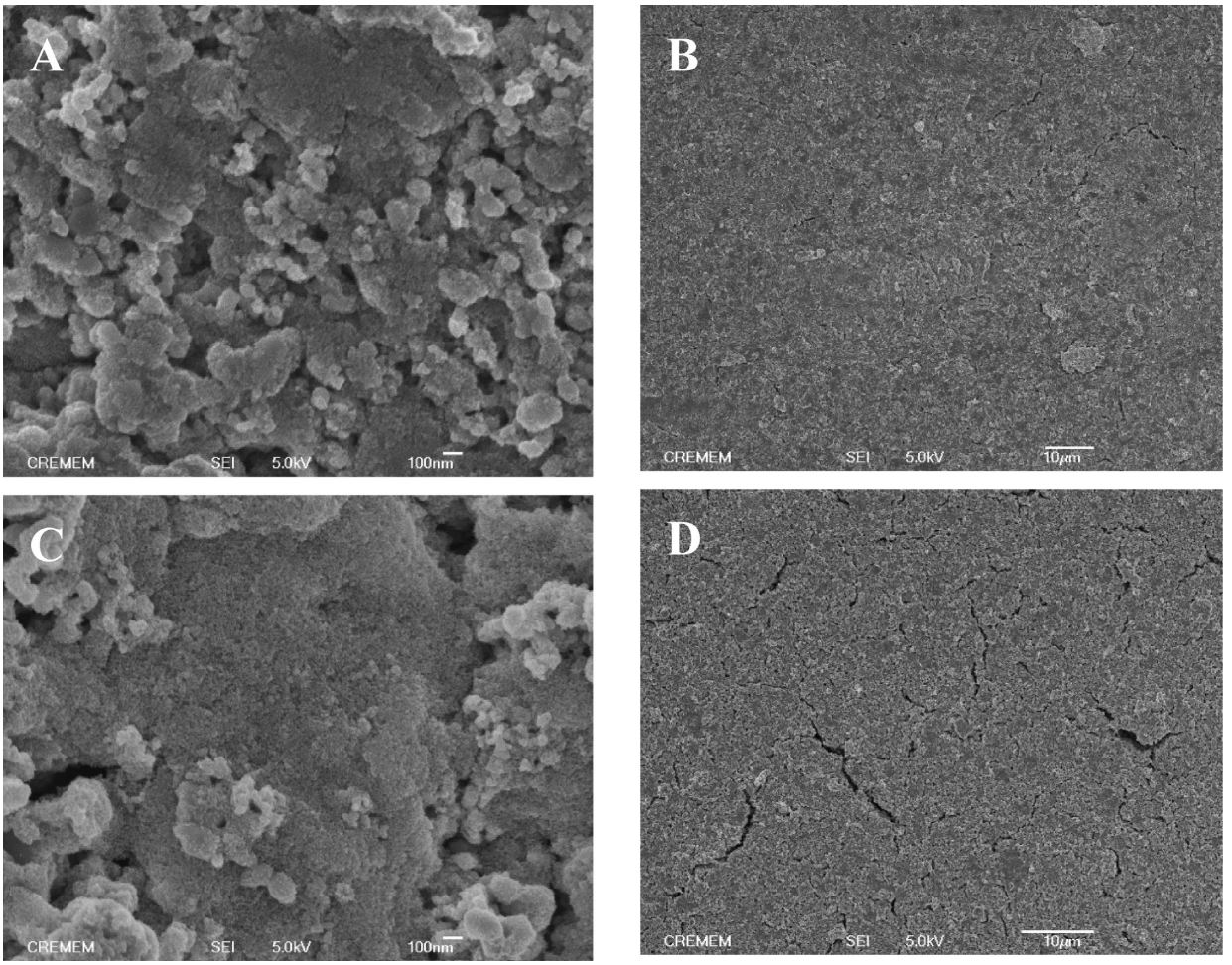

Figure 1. SEM images of UV-processed (A, B) and HT-treated (C, D) SnO_2 films made from SnO_2 nanoparticles with light-scattering particles.

Table 2. Textural Properties of the Scraped off Films As a Function of the Post-Treatment Determined from N_2 Sorption Measurements

sample[a]	S_{BET} ($m^2\ g^{-1}$)[b]	pore volume ($cm^3\ g^{-1}$)	pore size (nm)[c]
LT-treated film	3 ± 0.5	0.02 ± 0.002	21 ± 1
UV-treated film	61 ± 3.0	0.13 ± 0.005	8 ± 0.5
HT-treated film	48 ± 2.5	0.11 ± 0.005	9 ± 0.5

[a] LT: 150 °C for 2 h. UV: UV irradiation, HPL-N lamp 125 W for 3 h. HT: 450 °C for 30 min. [b] S_{BET}: BET specific surface area. [c] BJH model applied to the adsorption branch.

affecting the textural properties has occurred upon UV treatment. Moreover, the hysteresis loop observed in the N_2 adsorption−desorption isotherm revealed the presence of mesopores of average diameter of about 8 nm with a rather broad size distribution. In contrast, HT and LT treatments strongly affect the textural properties of the films. Thus, annealing at 450 °C induced a significant decrease in both BET specific surface area and pore volume. In addition, the LT treatment gave rise to a collapse of the textural properties of the films with a BET surface area and total pore volume of about 3 $m^2\ g^{-1}$ and 0.02 $cm^3\ g^{-1}$, respectively. As particle growth and sintering were very unlikely at tempertaures as low as 150 °C, this behavior could be related

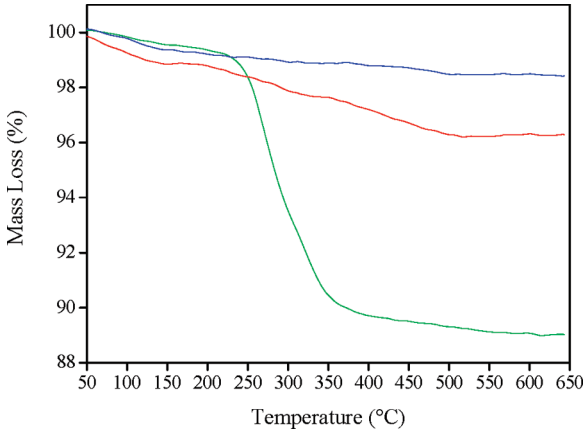

Figure 2. TG plots under an air flow of scraped off films treated at 150 °C (LT, green), at 450 °C (HT, blue), and under UV irradiation (red).

to the presence of large amounts of remaining organics provoking the agglomeration of the SnO_2 particles and pore blocking.

This was also assessed by TGA-MS measurements. Thus, a TGA curve in air of LT-treated layers scraped off exhibited a significant mass loss occurring in three main successive steps of 0.9% (from 20 to 230 °C), 8.9% (from 230 to 360 °C), and 1.2%

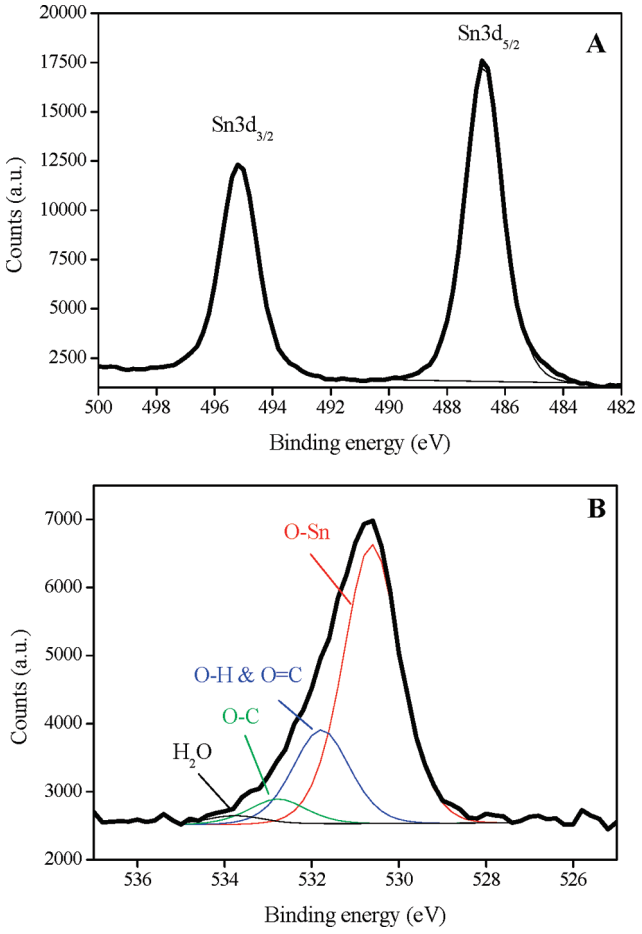

Figure 3. XPS spectrum of a UV-processed film; (A) Sn3d region; (B) O1s region with the corresponding fits.

(from 360 to 650 °C), yielding a final residue of 89% (Figure 2). The main species evolved during the pyrolysis process were water (m/z 17, 18), carbon dioxide (m/z 22, 44), acetic acid (m/z 60), acetone (m/z 58), and Triton X fragments as benzene (m/z 50, 51, 52, 77) that showed the incomplete removal of the organics present in the starting colloid. By contrast, the TGA curve of the UV-treated materials showed a much lower mass loss occurring in two main successive steps of 0.7 (from 20 to 200 °C) and 3.0% (from 200 to 450 °C) to yield a final residue of 96.3%. The main species detected by MS measurements were water (m/z 17, 18) and carbon dioxide (m/z 22, 44) that could be attributed to the release of adsorbed or structural water[31] and the decomposition of small amounts of residual organics. As a result, the UV treatment actually achieved the almost complete degradation of the surfactant and additives present in the starting colloidal solution and has enabled the preparation of mesoporous SnO_2 layers.

To have a better insight into the nature of the species and surface groups present in the films prepared, the scraped off UV- and HT-processed films were studied by XPS and FTIR. By XPS, tin and oxygen were detected in both cases along with carbon related to air pollution or residual carbon. The binding energy found for Sn $3d_{3/2}$ (486.7 eV) was the one expected for cassiterite tin dioxide (Figure 3A).[32] Analysis of the O 1s spectrum for the UV- and HT-processed films exhibited four signals at 530.6, 531.8, 532.8, and 533.8 ± 0.2 eV, which were

Table 3. Ratios of the Different XPS O1s Components after Fitting for UV- or HT-Treated SnO_2 Films

treatment	O−Sn	O−H and O=C	O−C	H_2O
UV processing	1.00	0.34	0.09	0.03
HT processing	1.00	0.22	0.12	0.01

Table 4. Comparison of the Photovoltaic Performance of the DSCs based on SnO_2 photoanodes after Various Post-Treatments[a]

conditions[b]	Th (μm)	J_{sc} (mA cm^{-2})	V_{oc} (V)	FF	PCE (%)
LT	1.3	0.7	0.38	0.53	0.15 ± 0.01
LT	3.6	2.3	0.34	0.53	0.41 ± 0.02
UV	1.3	3.7	0.51	0.50	0.94 ± 0.04
UV	2.2	6.3	0.48	0.50	1.51 ± 0.06
UV	3.6	10.5	0.45	0.48	2.27 ± 0.08
UV	4.5	12.6	0.41	0.44	2.27 ± 0.09
HT	1.3	3.9	0.44	0.40	0.69 ± 0.03
HT	3.6	11.0	0.38	0.38	1.59 ± 0.07

[a] Active surface area: 0.2 cm^2. Illumination: AM1.5G 100 mW cm^{-2}. Th: film thickness (± 0.1 μm). J_{sc}: short-circuit photocurrent density (± 0.05 mA cm^{-2}). V_{oc}: open-circuit photovoltage (± 0.005 V). FF: fill factor (± 0.01). PCE: power conversion efficiency. [b] LT: 150 °C for 2 h. UV: UV irradiation, HPL-N lamp 125 W for 3 h. HT: 450 °C for 30 min.

attributed to O−Sn bonds in SnO_2, O−H or O=C, or O−C and H_2O bonds, respectively (Figure 3B). The proportion of each group according to the kind of treatment used was assessed by integration of each component (Table 3). The contribution of the band detected at 531.8 eV was found to be higher in the UV-processed film than that of the HT-sintered layer. As a careful analysis of the carbon indicated that the C=O contribution was similar in both samples, this finding can be related to a more hydroxylated surface after UV treatment. Consequently, the data revealed that the UV-processed films contained much more hydroxyl groups than the HT-treated ones. This was consistent with FTIR data (not shown) that indicated a higher contribution of the stretching vibration bands of O−H (3400−3000 cm^{-1}) and Sn−O bonds of Sn−OH groups (shoulder at 540 cm^{-1}) in the spectrum of UV-treated films than that of its HT-processed analogue.

Photoelectrochemical Behavior of SnO_2-Based Cells. After dye-sensitization with the N3 dye, the photoelectrochemical responses of the UV-processed photoanodes were tested under AM1.5G irradiation (100 mW cm^{-2}) using a commercial iodide−iodine based liquid electrolyte and compared to that of LT- and HT-processed films. The corresponding photovoltaic data are gathered in Table 4. LT-treated films led to very weak power conversion efficiencies, i.e., < 0.5%, that can be related to their poor textural properties. On the other hand, UV-processed sensitized films led to higher efficiencies than those sintered at high temperature mainly due to a significant improvement of the open-circuit voltage (V_{oc}) and fill factor (FF) values. This trend was previously observed for TiO_2 layers thinner than 2 μm fabricated from different precursors.[29] For instance, for 3.6 μm thick layers, the UV-processed SnO_2 photoanodes yielded an overall power conversion efficiency (η) of 2.27 ± 0.08% with a short-circuit photocurrent density (J_{sc}) of 10.5 ± 0.05 mA cm^{-2}, an open-circuit photovoltage (V_{oc}) of 0.45 ± 0.005 V, and a fill

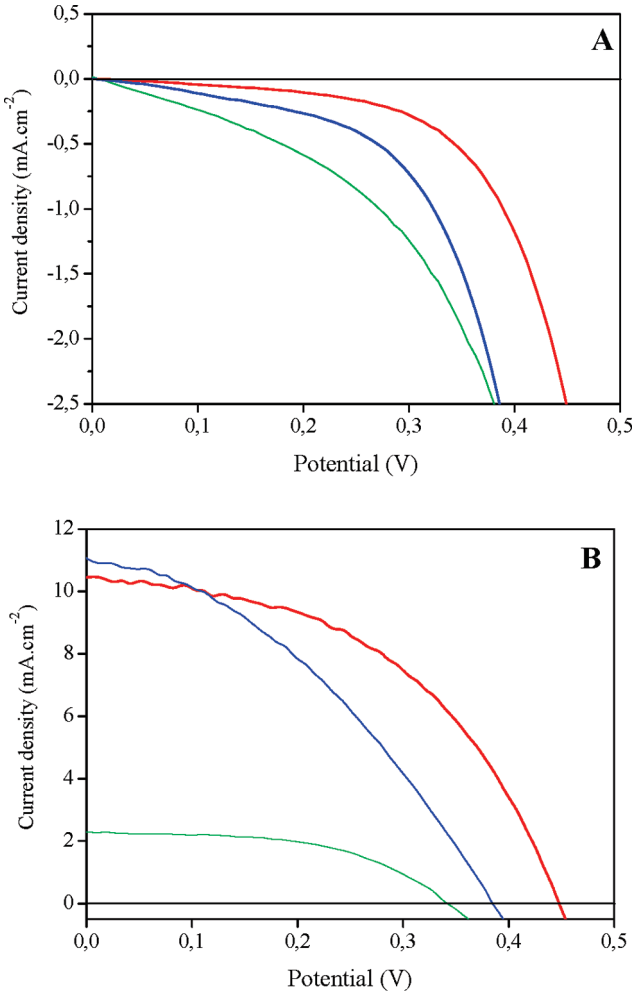

Figure 4. Current−voltage curves for a N3-sensitized DSC with a 3.6 μm thick SnO_2 film treated at 150 °C (LT) (green), a N3-sensitized DSC with a 3.6 μm thick SnO_2 film treated at 450 °C (HT) (blue), a N3-sensitized DSC with a 3.6 μm thick SnO_2 film treated under UV irradiation (UV) (red); (A) in the dark; (B) under AM1.5G illumination at 100 mW cm^{-2}.

factor (FF) of 0.48 ± 0.01 (Figure 4B). In this case, the IPCE plot showed a quantum yield higher than 40% in the 400−600 nm wavelength range with a maximum of 51% at 517 nm (Figure 5). In comparison, annealing at 450 °C led to a power conversion efficiency more than 40% lower, whereas the corresponding IPCE curve is similar to that of the UV-treated sample accounting for the close short-circuit photocurrent density (J_{sc}) values. It is also worth mentioning that the same trend was found for thin porous anodes only made of SnO_2 nanoparticles. Thus, 1 μm thick UV-treated films processed from the commercial SnO_2 colloid without light scattering particles gave rise to better efficiencies, i.e., 0.65 ± 0.03%, than those of the corresponding analogue annealed at 450 °C, i.e., 0.26 ± 0.02%, mainly due to improved open-circuit photovoltage (0.54 vs 0.41 ± 0.005 V) and fill factor (0.58 vs 0.38 ± 0.01).

To the best of our knowledge, the previous results are among the highest reported so far for pure SnO_2-based DSCs.[21,25,27] However, attempts to enhance the performances by increasing the film thickness remained unsuccessfull. Indeed, the power conversion efficiency reached a plateau value, i.e., 2.27%, for a

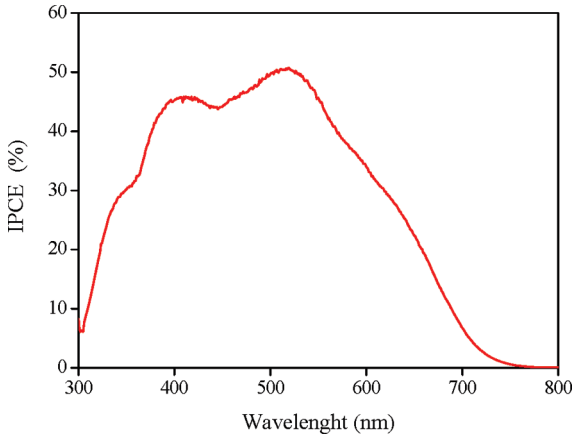

Figure 5. Incident photon-to-current efficiency (IPCE) of a N3-sensitized DSC with a 3.6 μm thick SnO_2 film treated under UV irradiation.

3.5−5 μm thick UV-treated film and decreased for thicker layers due to a collapse of the short-circuit photocurrent density and the open-circuit photovoltage. That pointed out the increasing importance of electronic limitations arising from resistive losses. Two explanations may be proposed to rationalize this behavior: (i) weak electron diffusion and transport in the porous layer, and (ii) poor electrolyte diffusion within the porous layer inhibiting a fast regeneration of the system.

Nonetheless, regardless of the SnO_2 particle nature, these studies clearly evidence the beneficial effect of the UV-treated films compared to the HT-sintered ones for film thickness below 4 μm because the efficiencies were higher mostly due to higher V_{oc} and FF values. This was therefore in favor of lower recombination phenomena in the UV-processed layers that might be related to the presence of more surface hydroxyl groups or less traps.

To confirm the latter assumption, changes in the dark recombination current with the applied potential were examined (Figure 4A). This current is correlated to the recombination of electrons with the redox mediator. The onset of dark current took place at a higher potential for UV-treated electrodes compared to the HT-processed films. The presence of fewer traps in the UV layers, whose energy shifts with the applied bias, might decrease the charge leakage in the UV-treated electrodes. Moreover, the bias-induced increase in the electron recombination rates is one of the possible origins of the lower fill factor of the HT-processed films. Thus, higher recombination reactions decrease the electron density in the semiconducting film, which provokes a decrease in the resulting open-circuit photovoltage.

Another method to probe the recombination rates is to monitor the V_{oc} rise or decay between the dark equilibrium and the illuminated steady state.[33] According to this reference, an accurate recombination lifetime constant could be determined from the equation: $\tau_n = -(k_B T)/(q)[(dV_{oc})/(dt)]^{-1}$. Following this methodology, we can evidence that the electron lifetime in the UV-processed SnO_2 layers was higher for the low V_{oc} value (Figure 6). It implies a weaker recombination rate for UV-processed SnO_2 films, which is consistent with the results reported in Table 4, where V_{oc} is greater for UV-treated samples than for calcined ones. That reveals that either the disorder and/or impurities amount is reduced in UV-treated films. Furthermore, Figure 7 depicts the Nyquist plots obtained by electrical impedance spectroscopy (EIS) for dye-sensitized solar cells prepared by UV and HT treatments. For the UV-treated layers,

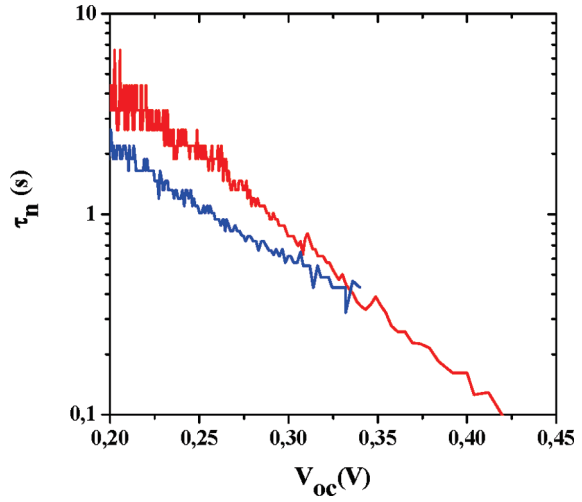

Figure 6. Charge carrier lifetime for (blue) a N3-sensitized DSC with a 3.6 μm thick SnO_2 film on glass sintered at 450 °C, (red) a N3-sensitized DSC with a 3.6 μm thick SnO_2 film on glass treated under UV irradiation. Lifetimes have been calculated from V_{oc} decay experiments with eq 6 of ref 33.

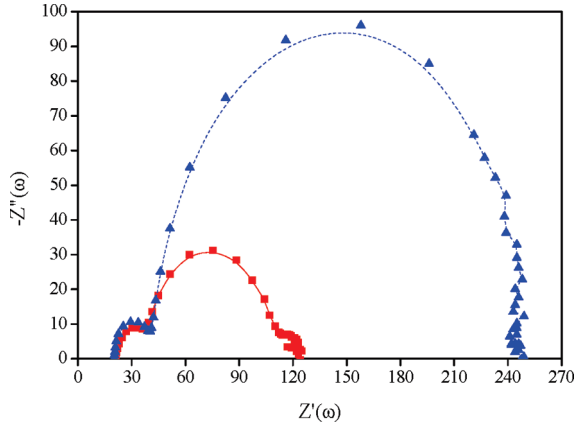

Figure 7. Electrical impedance spectra for (up triangle, blue-dashed line) a N3-sensitized DSC with a 3.6 μm thick SnO_2 film on glass sintered at 450 °C; (square, red full line) a N3-sensitized DSC with a 3.6 μm thick SnO_2 film on glass treated under UV irradiation.

three hemispheres were observed from the Nyquist plot. These features can be assigned as follows.[34] (1) The semicircle in the high-frequency region (in the kHz range) represents the charge-transfer at the platinum counter-electrode. (2) The intermediate-frequency peak (in the 10−100 Hz range) reflects the phenomenon at the SnO_2/electrolyte interface. (3) The low-frequency feature (in the mHz range) corresponds to the Nernst diffusion of the electrolyte. In contrast, HT treatment led to considerable enlargment of the medium frequency semicircle along with a featureless low frequency semicircle. This might be related to higher resistances in the calcined samples, which is in agreement with the lower V_{oc} and FF compared to the UV-processed SnO_2-based cells (Table 4).

The origin of the improved photovoltaic performances of UV-processed photoanodes can be rationalized as follows. According to SEM and N_2 sorption analyses, UV-treated layers showed higher surface area and porosity and a crack-free surface morphology compared to those of the HT-sintered analogues. However, these features that mainly rule the short-circuit photocurrent density value (dye amount and regeneration) do not seem to be the key parameters at the origin of the better performances of the UV-treated systems. Indeed, for the same film thickness, both treatments led to close short-circuit photocurrent densities. A better nanoparticle connection and film adhesion to the conductive substrate could thus offset the lower textural properties for annealed films. By contrast, the UV-processing method improved significantly both open-circuit photovoltage and fill factor and induced a significant decrease in the dark current. The increase in open-circuit photovoltage can stem from the change in the surface state of the SnO_2 semiconductor that favors to shift the Fermi level toward a negative potential. Moreover, as shown by the weaker dark current and higher fill factor, these surface states in UV-treated layers enables diminishing the recombination rate as highlighted by V_{oc} decay analyses.

CONCLUSION

In summary, we have demonstrated that the direct UV irradiation, without any further thermal or chemical treatment, of SnO_2 films prepared by the "doctor-blade" technique, provides nanoporous SnO_2 electrodes that include more surface hydroxyl groups than the calcined analogues. After dye-sensitization, the 1−5 μm thick layers show excellent photovoltaic responses with maximum overall power conversion efficiency of 2.27% under AM1.5G illumination at 100 mW cm^{-2}. These performances were better than those found or previously reported for pure SnO_2 films annealed at high temperature due to higher V_{oc} and FF. Slower recombination rates along with more hydroxylated SnO_2 layers would be at the origin of the improved performances of the UV-processed SnO_2 films. This route is therefore suitable for plastic electronics and can be very useful in the field of gas sensing and antistatic coatings.

AUTHOR INFORMATION

Corresponding Author

*E-mail: t.toupance@ism.u-bordeaux1.fr.

ACKNOWLEDGMENT

Mrs. Elisabeth Sellier and Odile Babot (University of Bordeaux 1) are acknowledged for the scanning electron microscopy measurements and nitrogen sorption analyses, respectively. The authors thank the CNRS (Programme Interdisciplinaire Energie, PR-09-2.1.1-2, Nanodisflex), the Aquitaine Region (ZT PhD fellowship), and the "Agence Nationale de la Recherche" (Contract ANR-05-PV-008-14).

REFERENCES

(1) O' Regan, B.; Grätzel, M. *Nature* **1991**, *353*, 737–740.

(2) (a) Grätzel, M. *Acc. Chem. Res.* **2009**, *42*, 1788–1798. (b) Hagfeldt, A.; Boschloo, G.; Sun, L.; Kloo, L.; Pettersson, H. *Chem. Rev.* **2010**, *110*, 6595–6663.

(3) (a) Grätzel, M. *J. Photochem. Photobiol. A: Chem.* **2004**, *164*, 3–14. (b) Nazeeruddin, M. K.; De Angelis, F.; Fantacci, S.; Selloni, A.; Viscardi, G.; Liska, P.; Ito, S.; Takeru, B.; Grätzel, M. *J. Am. Chem. Soc.* **2005**, *127*, 16835–16847. (c) Gao, F.; Wang, Y.; Shi, D.; Zhang, J.; Wang, M.; Jing, X.; Humphry-Baker, R.; Wang, P.; Zakeeruddin, S. M.; Grätzel, M. *J. Am. Chem. Soc.* **2008**, *130*, 10720–10728.

(4) Han, L.; Fukui, A.; Chiba, Y.; Islam, A.; Komiya, R.; Fuke, N.; Koide, N.; Yamanaka, R.; Shimizu, M. *Appl. Phys. Lett.* **2009**, *94*, 013305-1–013305-3.
(5) Pagliaro, M.; Ciriminna, R.; Palmisano, G. *Chem. Sus. Chem.* **2008**, *1*, 880–891.
(6) Murakami, T. N.; Kijitori, Y.; Kawashima, N.; Miyasaka, T. *J. Photochem. Photobiol. A: Chem.* **2004**, *164*, 187–191.
(7) (a) Gutierrez-Tauste, D.; Zumeta, I.; Vigil, E.; Hernandez-Fenollosa, M. A.; Domenech, X.; Ayllon, J. A. *J. Photochem. Photobiol. A: Chem.* **2005**, *175*, 165–171. (b) Zhang, D.; Yoshida, T.; Oekermann, G.; Furuta, K.; Minoura, H. *Adv. Funct. Mater.* **2006**, *16*, 1228–1234.
(8) (a) Longo, C.; Freitas, J.; DePaoli, M. A. *J. Photochem. Photobiol. A: Chem.* **2003**, *159*, 33–39. (b) Lewis, L. N.; Spivack, J. L.; Gasaway, S.; Williams, E. D.; Gui, J. Y.; Manivannan, V.; Siclovan, O. P. *Sol. Energy Mater. Sol. Cells* **2006**, *90*, 1041–1051.
(9) Zhang, D.; Yoshida, T.; Furuta, K.; Minoura, H. *J. Photochem. Photobiol. A: Chem.* **2004**, *164*, 159–166.
(10) (a) Park, N.-G.; Kim, K. M.; Kang, M. G.; Ryu, K. S.; Chang, S. H.; Shin, Y.-Y. *Adv. Mater.* **2005**, *17*, 2349–2353. (b) du Pasquier, A.; Stewart, M.; Spitler, T.; Coleman, M. *Sol. Energy Mater. Sol. Cells* **2009**, *93*, 528–535.
(11) Stathatos, E.; Chen, Y.; Dionysiou, D. D. *Sol. Energy Mater. Sol. Cells* **2008**, *92*, 1358–1365.
(12) Uchida, S.; Tomiha, M.; Takizawa, H.; Kawaraya, M. *J. Photochem. Photobiol. A: Chem.* **2004**, *164*, 93–96.
(13) Kim, H.; Auyeung, R. C. Y.; Ollinger, M.; Kushto, G. P.; Kafafi, Z. H.; Piqué, A. *Appl. Phys. A: Mater. Sci. Process.* **2006**, *83*, 73–76.
(14) Pichot, F.; Pitts, J. R.; Gregg, B. A. *Langmuir* **2000**, *16*, 5626–5630.
(15) Weerasinghe, H. C.; Sirimanne, P. M.; Simon, G. P.; Cheng, Y. B. *Sol. Energy Mater. Sol. Cells* **2009**, *206*, 64–70.
(16) (a) Lindström, H.; Holmberg, A.; Magnusson, E.; Lindquist, S.-T.; Malmqvist, L.; Hagfeldt, A. *Nano Lett.* **2001**, *1*, 97–100. (b) Halme, J.; Saarinen, J.; Lund, P. *Sol. Energy Mater. Sol. Cells* **2006**, *90*, 887–899. (c) Yamaguchi, T.; Tobe, N.; Matsumoto, D.; Arakawa, H. *Chem. Commun.* **2007**, 4767–4769.
(17) (a) Grinis, L.; Dor, S.; Ofir, A.; Zaban, A. *J. Photochem. Photobiol. A: Chem.* **2008**, *198*, 52–59. (b) Grinis, L.; Dor, S.; Ofir, A.; Zaban, A. *Adv. Funct. Mater.* **2010**, *20*, 282–288.
(18) Tan, W.; Chen, J.; Zhou, X.; Zhang, J.; Lin, Y.; Li, X.; Xiao, X. *J. Solid State Electrochem.* **2009**, *13*, 651–656.
(19) Hendry, E.; Koeberg, M.; O'Regan, B.; Boon, M. *Nano Lett.* **2006**, *6*, 755–759.
(20) (a) Gordon, R. G. *MRS Bull.* **2000**, *25*, 52–58. (b) Boegeat, D.; Jousseaume, B.; Toupance, T.; Campet, G.; Fournès, L. *Inorg. Chem.* **2000**, *39*, 3924–3927. (c) Toupance, T.; Babot, O.; Jousseaume, B.; Vilaça, G. *Chem. Mater.* **2003**, *15*, 4691–4697. (d) Toupance; El Hamzaoui, H.; Jousseaume, B.; Riague, H.; Saadeddin, I.; Campet, G.; Brötz, J. *Chem. Mater.* **2006**, *18*, 6364–6372.
(21) (a) Kay, A.; Grätzel, M. *Chem. Mater.* **2002**, *14*, 2930–2935. (b) Green, A. N. M.; Palomares, E.; Haque, S.; Kroon, J. M.; Durrant, J. R. *J. Phys. Chem. B* **2005**, *109*, 12525–12533. (c) Fukai, Y.; Kondo, Y.; Mori, S. *Electrochem. Commun.* **2007**, *9*, 1439–1443.
(22) Vilaça, G.; Jousseaume, B.; Mahieux, C.; Belin, C.; Cachet, H.; Bernard, M.-C.; Vivier, V.; Toupance, T. *Adv. Mater.* **2006**, *18*, 1073–1077.
(23) Chappel, S.; Zaban, A. *Sol. Energy Mater. Sol. Cells* **2002**, *71*, 141–152.
(24) (a) Liu, J.; Luo, T.; Mouli, S.; Meng, F.; Sun, B.; Li, M.; Liu, J. *Chem. Commun.* **2010**, *46*, 472–474. (b) Ramasamy, E.; Lee, J. *J. Phys. Chem. C* **2010**, *114*, 22032–22037.
(25) Gubbala, S.; Chakrapami, V.; Kumar, V.; Sunkara, M. K. *Adv. Funct. Mater.* **2008**, *18*, 2411–2418.
(26) (a) Qian, J.; Liu, P.; Xiao, Y.; Jiang, Y.; Cao, Y.; Ai, X.; Yang, H. *Adv. Mater.* **2009**, *21*, 3363–3667. (b) Wang, Y.-F.; Li, J.-W.; Hou, Y.-F.; Yu, X.-Y.; Su, C.-Y.; Kuang, D.-B. *Chem. Eu. J.* **2010**, *16*, 8620–8625.
(27) Lee, J.-H.; Park, N.-G.; Shin, Y.-J. *Sol. Energy Mater. Sol. Cells* **2011**, *95*, 179–183.
(28) Tebby, Z.; Babot, O.; Toupance, T.; Park, D.-H.; Campet, G.; Delville, M.-H. *Chem. Mater.* **2008**, *20*, 7260–7267.
(29) Tebby, Z.; Babot, O.; Michau, D.; Hirsch, L.; Carlos, L.; Toupance, T. *J. Photochem. Photobiol. A: Chem.* **2009**, *205*, 70–76.
(30) Mazille, F.; Frei, Z.; Kuang, D.; Zhao, D.; Zakeeruddin, S. M.; Grätzel, M.; Dyson, P. J. *Inorg. Chem.* **2006**, *45*, 1585–1590.
(31) Gamard, A.; Babot, O.; Jousseaume, B.; Rascle, M.-C.; Toupance, T.; Campet, G. *Chem. Mater.* **2000**, *12*, 3419–3426.
(32) Ahn, H.-J.; Choi, H.-C.; Park, K.-W.; Kim, S.-B.; Sung, Y.-E. *J. Phys. Chem. B* **2004**, *108*, 9815–9820.
(33) Zaban, A.; Greenshtein, M.; Bisquert, J. *Chem. Phys. Chem.* **2003**, *4*, 859–864.
(34) Kern, R.; Sastrawan, R.; Ferber, J.; Stangl, R.; Luther, J. *Electrochim. Acta* **2002**, *47*, 4213–4225.